Computation of the Shuttle Solid Booster Nozzle Start-Up Transient Flow

Michael C. Cline*

Los Alamos National Laboratory, Los Alamos, New Mexico

and

Richard G. Wilmoth†

NASA Langley Research Center, Hampton, Virginia

The first NASA Space Shuttle flight (STS-1) produced an overpressure wave that exceeded preflight predictions by as much as 5 to 1. This second overpressure wave occurred just after the first overpressure wave produced by the solid rocket booster igniter. To understand this second overpressure phenomenon, a numerical simulation effort was undertaken. Both the SRB static firing test and STS-1 geometries were studied for two-dimensional (axisymmetric), inviscid and viscous flow. The inviscid calculations did not produce significant second overpressure waves. However, the viscous calculations did produce second overpressure waves that qualitatively agree with experiment. These overpressure waves were present in both the static firing test and STS-1 geometries. This second overpressure wave is generated by the motion of the boundary-layer separation point and the subsequent radial motion of the exhaust jet during the start-up of the SRB nozzle flow. The presence of the mobile launch platform exhaust hole wall amplifies this wave, but does not appear to be the source of any additional overpressure waves. The lack of good quantitative agreement between theory and experiment indicates that other overpressure sources, not accounted for by this simulation, may be present.

Introduction

THE first NASA Space Shuttle flight (STS-1) produced an overpressure wave that exceeded preflight predictions by as much as 5 to 1.[1] This overpressure wave occurred just after ignition of the solid rocket boosters (SRB). The first wave produced was the igniter wave which, although relatively large in amplitude, was very short in duration and of minor concern. The second overpressure wave occurred shortly after the igniter wave and was greater in magnitude and much longer in duration, producing significant differential pressures and deflections on various vehicle components. Such overpressures could possibly damage the Shuttle Orbiter itself or its payload. Extensive ground testing and analysis provided an engineering fix that has worked successfully on all subsequent launches. Additional water jets were installed in the mobile launch platform (MLP) SRB exhaust holes, and caps were placed on the top of the portion of the SRB exhaust holes not covered by the SRB nozzles. These modifications to the MLP significantly reduced the overpressure on the Orbiter during the second flight (STS-2). However, these modifications did not eliminate the overpressure but merely contained it inside the MLP. Because the cause or source of the overpressure had not been fully determined, any modifications that may be made to the MLP in the future could result in an increase in the overpressure. In addition, the use of a different MLP, such as the one to be used by the U.S. Air Force, might produce totally different results.

As a result of the interest to understand this phenomenon, a numerical simulation effort was undertaken jointly by the NASA Langley Research Center and the Los Alamos National Laboratory. This effort involved using a modified version of the two-dimensional VNAP2 code[2,3] to analyze the start-up transient of the SRB nozzle flow. The VNAP2 code solves the two-dimensional (axisymmetric), time-dependent, compressible, turbulent flow equations for flow in and about relatively general nozzle-afterbody configurations.

Studies of the transient pressure waves during the start-up of a rocket motor have included one-dimensional linearized wave equation analysis,[4-6] two-dimensional, inviscid, compressible flow calculations,[7,9] and two-dimensional, viscous (laminar), compressible flow.[10] The work of Ref. 10 differs from the present work in that it used a more simplified geometry, neglected the subsonic part of the SRB nozzle, assumed laminar flow, employed an extremely course downstream grid, and did not include the SRB static firing case.

Flow Geometry

Two different flow geometries were considered. The first is the static firing configuration (see Fig. 1), without the presence of the MLP. This geometry represents an isolated SRB that had been fired statically and for which experimental data were available. The computational region for the numerical simulation is outlined by the dashed line. This case is of special interest because the experimental data indicated that a small second overpressure wave occurred without the presence of the MLP. The actual computational region for this case is shown in Fig. 2. The upper, right, and left-upper boundaries are arbitrary computational boundaries, the lower boundary is the nozzle centerline or axis of symmetry, and the lower-left boundary is the nozzle inflow boundary. The upper and right boundaries were located such that any waves that might reflect from these boundaries would not return to the overpressure wave region during the time interval of interest. The left-upper boundary location was required, by the VNAP2 code,[2] to be the same as the nozzle inlet boundary (left-lower boundary). The nozzle throat and exit radii are 69.1 cm (27.2 in.) and 185 cm (72.8 in.), respectively, while the radius of the outer computational boundary is 1524.0 cm (600.0 in.). The nozzle length (throat to exit) is 365.0 cm (143.7 in.), while the length of the computational

region is 1895.4 cm (746.2 in.). Figure 2 shows how the nozzle external shroud was approximated in order to produce a smoother grid above the nozzle. The computational grid for the static firing case is shown in Fig. 3.

The second case is the STS-1 configuration which includes the SRB exhaust hole wall in the MLP, as shown in Fig. 1. The computational region is again shown by the dashed lines. The actual computational region for the STS-1 case is shown in Fig. 4. The upper boundary is now a solid wall except for the short section just above the nozzle that is an arbitrary computational boundary. The actual SRB exhaust hole is rectangular in cross section with the SRB nozzle located at one end. The side walls are 308.6 cm (121.5 in.) from the nozzle centerline, while the end wall is 358.5 cm (141.1 in.). In order to arrive at a single distance as required by the two-dimensional calculation, a length of 327.4 cm (128.91 in.) was used, which is approximately the average of the distance to the two side walls and the one end wall. The wall in the actual MLP is only one-half as long as that in Fig. 4. However, one of the side walls has a flame deflector that acts as a continuation of the wall. Therefore, it was not clear whether the simulated MLP wall should be one-half the length of that in Fig. 4 as is the actual end wall or continue to the right boundary like one of the actual side walls. In order to simulate the worst case, the MLP wall was assumed to end at the right boundary. The computational grid for the STS-case is similar to the lower one-third for the static firing case, shown in Fig. 3.

Fluid Model

The flow in a rocket nozzle during start-up is characterized by highly transient turbulent flow with both a separated boundary layer and subsequent free shear layer. To model such a complex flow, the unsteady two-dimensional, compressible, Navier-Stokes equations were used. Because it is not clear how to use a mixing-length turbulence model approach for both a separated boundary layer and free shear layer, the Jones-Launder[11] two-equation turbulence model was employed. VNAP2 employs an explicit artificial viscosity, modeled after the Navier-Stokes equations, to stabilize the calculations for shock waves. This artificial viscosity is used in place of the fourth-order smoothing usually employed by Hung and MacCormack.[12] The fluid was assumed to be an ideal gas. A complete description of the governing equations, including the turbulence model, is given in Ref. 2.

Numerical Method

The physical space grid, shown in Fig. 3, is mapped into and equal-spaced rectangular computational space grid. For details of this transformation see Ref. 2. The grid is then divided into interior (includes the axis of symmetry) and boundary points. The boundary points are further divided into left-lower (nozzle inlet), left-upper (top of MLP hole in

STS-1 case), upper (MLP hole wall in the STS-1 case), and right boundaries.

Interior Grid Points

The interior grid points are computed using the unsplit MacCormack scheme.[13] The governing equations are left in nonconservation form. In order to improve the computational efficiency for this high Reynolds number flow, the grid points in the fine part of the grid are subcycled. This is accomplished by first computing the grid points in the coarse part of the grid for one time step Δt. Next, the grid points in the fine grid are calculated k times, where k is an integer, with a time step $\Delta t/k$. The grid points at the edge of the fine grid require a special procedure because one of their
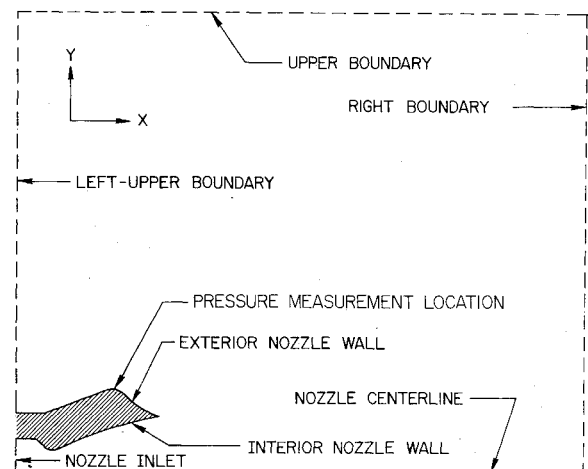

Fig. 2 Computation region for the static firing case showing the approximated SRB external nozzle contour and boundary labels.
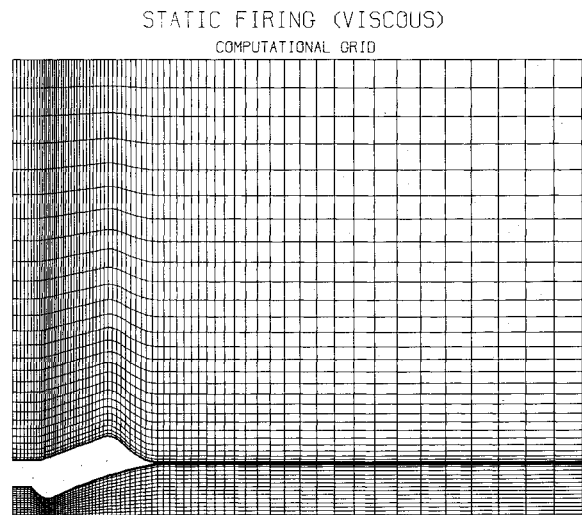

Fig. 3 Computational grid for the static firing case.
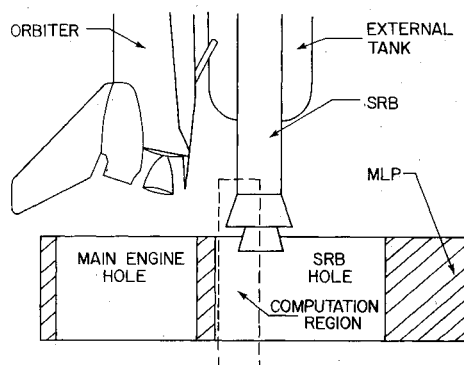

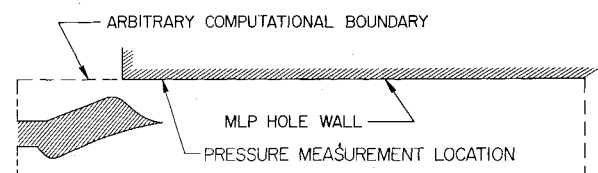Fig. 1 Computation region geometry.

Fig. 4 Computation region for the STS-1 case showing the MLP hole wall.

neighboring points is calculated as part of the coarse grid. Except for the first subcycled time step, this point is unknown. However, the values at t and $t + \Delta t$ are known from the coarse grid solution, therefore, the values between t and $t + \Delta t$ are determined by linear interpolation. This procedure preserves the time accuracy and usually reduces the computational time by factor of approximately 2.

The axis of symmetry grid points are also calculated by the interior point scheme assuming flow symmetry.

Left-Lower Boundary Grid Points

The left-lower boundary is the SRB nozzle inlet. The boundary condition is the specification of the total pressure p_T and total temperature T_T as a function of time. The actual values of p_T and T_T, used in both the static firing and STS-1 cases, are shown in Fig. 5. The p_T values are for the QM-3 static firing case (unpublished Thiokol data) and are very similar to the STS-1 values in Ref. 14. The values of T_T were determined by the procedure in Ref. 15 and again are similar to those in Ref. 14. The third boundary condition is the specification of the flow angle θ, which is set to 0. From the specified values of p_T, T_T, and θ, a characteristic scheme is used to calculate the x-direction velocity component u, the y-direction velocity component v, the pressure p, and the density ρ. The viscous terms are treated as source terms. For details of the method, see Ref. 2.

Left-Upper Boundary Grid Points

This boundary is the most important arbitary boundary. For the static case, the pressure was measured at the downstream tip of the nozzle shroud which is very close to this boundary. Waves reflected back into the computational region from this boundary will mask the true pressure-time history at the shroud tip. In the STS-1 case, one of the pressure transducers was located at the top of the MLP hole which is also very close to this boundary.

To determine how this boundary should be treated, a separate boundary condition study was undertaken. This study consisted of subsonic flow in a duct with a prescribed pressure pulse at the right end and several different boundary conditions applied at the left end. For inflow—flow from left to right—the following five boundary conditions were considered: 1) specify p_T, T_T, and θ; 2) specify u, v, and ρ; 3) specify p, v, and ρ; 4) and specify v and ρ while determining u using the nonreflecting condition based on the ideas of Rudy and Strikwerda[16]; and 5) specify v and ρ while determining p using a similar nonreflecting condition. For outflow—flow from right to left—the two boundary conditions are as follows: 1) the specification of p and 2) the determination of p using the procedure of Ref. 16. All nonspecified quantities were computed using a characteristic scheme. The viscous terms were treated as source terms. For details of these boundary condition treatments, see Ref. 2.
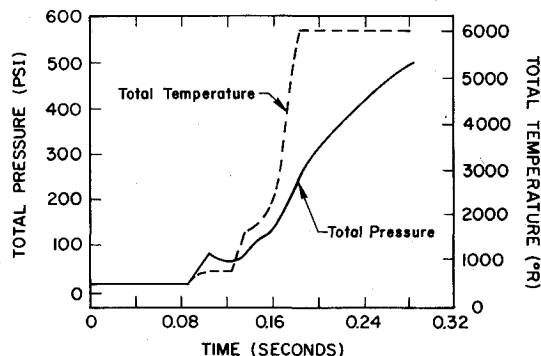
A typical calculation is shown in Fig. 6. The flow is moving in a duct from left to right with a Mach number of 0.1 and atmospheric pressure and temperature. Each frame is the pressure-time history at a grid point halfway between the left and right ends and N is the number of time steps. In the top frame, the left end boundary condition is the specification of u, v, and ρ. From this frame it can be seen that the wave passing by from right to left is reflected by the left end boundary condition and passes again, this time from left to right. In the second frame, the boundary condition is the specification of p, v, and ρ. This produces a reflection similar to the preceding case, except the reflected wave is inverted. In the third frame, the boundary condition is the specification of p_T, T_T, and θ. From this frame it an be seen once again a reflected wave appears. There has been some confusion in the literature as to whether specifying p_T causes reflections. Because p_T is not constant in a time-dependent flow and, therefore, is an unknown quantity that is part of the solution, specifying it as a constant will cause reflections as shown above. In fact, for this case, the p_T boundary condition reflection is very similar to the p, v, and ρ boundary condition reflections. This is because the Mach number is very low and, therefore p is approximately equal to p_T. This fact, combined with the observation that there is insufficient time for the pressure wave to significantly alter the flow velocity and, therefore, the Mach number, results in a p that is very nearly constant although it is p_T that is being held constant. For a further discussion of these points, see Ref. 2. The bottom frame is the nonreflecting boundary condition (item 5 above) and, as can be seen, does cancel the reflection.

The preceding results are for plane waves in a constant-area duct and are, therefore, one-dimensional. Two-dimensional waves, i.e., waves not moving perpendicular to the boundary, are not exactly canceled by this procedure, but their reflections are significantly reduced in magnitude. Attempts to develop a procedure that would cancel all two-dimensional waves did not produce a significant reduction in the magnitude of the reflections when compared to the one-dimensional procedure. Due to time limitations, this work was set aside for consideration at some future time.

Based on the results of this study, the following boundary conditions were employed: Inflow: specify v and ρ, calculate p from the nonreflecting condition and calculate u from the characteristic scheme; outflow: calculate p from the nonreflecting condition and calculate v, ρ, and u from the characteristic scheme. While the above boundary conditions were felt to be superior to the other boundary conditions considered, static firing case calculations were made using all boundary conditions to test the sensitivity of the results to these different boundary conditions. While the results from these various boundary conditions differed in detail, they all produced the same overall qualitative features of the flow.

Upper Boundary Grid Points

For the static firing case, this boundary is an arbitrary computational boundary. For the STS-1 case, most of this boundary is the MLP hole wall and was treated as a free-slip boundary. The short upstream part (see Fig. 4) is an arbitary computational boundary. The arbitrary computational boundary is treated following the procedure for the left-upper boundary with u and v changing roles. For the free-slip wall boundary (STS-1) v is set equal to zero, while u, p, and ρ are calculated using a characteristic scheme with the viscous terms treated as source terms. For details of this procedure, see Ref. 2.

Right Boundary Grid Points

The right boundary is also an arbitrary computational boundary. The boundary condition was the same as the left-upper boundary with the one exception being that when the exiting flow went supersonic the boundary condition would

Fig. 5 Total pressure p_T and total temperature T_T vs time in the SRB chamber.

switch to zeroth-order extrapolation of all variables. However, when the Mach disk moved across this boundary, the procedure became unstable. Because this problem occurred at a time when disturbances from this boundary would not reach the overpressure wave region during the time interval of interest, the boundary condition switched to extrapolation for all right boundary grid points regardless of the Mach number just as the Mach disk approached the boundary. This procedure was kept in force for the rest of the calculation.

Interior/Exterior Nozzle Wall Grid Points

The boundary condition on this wall was the no-slip condition, i.e., $u = v = 0$. The wall was assumed to be adiabatic. Therefore, p and ρ were calculated using a characteristic scheme with the temperature gradient normal to the wall set equal to zero. The viscous terms were treated as source terms. The turbulence model boundary conditions set the turbulence energy and the gradient of the dissipation rate to zero. For details of these boundary conditions, see Ref. 2.

Grid Point Distribution

Three different grid point distributions were employed for the static firing case. The first calculation consisted of the flow in the interior of the SRB nozzle. The minimum spacing adjacent to the nozzle wall was 0.127 cm (0.05 in.). The second static firing case runs included the region shown in Fig. 2 with a minimum spacing adjacent to the nozzle wall of 0.508 cm (0.2 in.). The final grid, shown in Fig. 3, employed the 0.508 cm spacing adjacent to the wall, but used a much finer grid spacing in the x direction just downstream of the nozzle exit. All three grids produced the same overall qualitative features of the flow.

It should be noted that, for a steady-state calculation, a finer grid adjacent to the wall would be desirable. However, for the transient case with such massive separation, it is not obvious that the finest details of the boundary-layer flow upstream of the separation point region need to be resolved to accurately predict the dynamics of the separated boundary layer and subsequent free-shear layer.
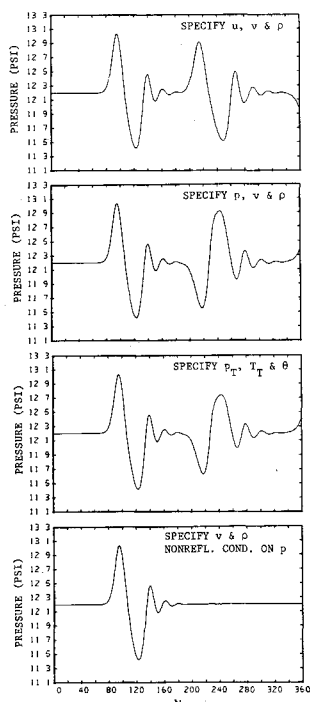
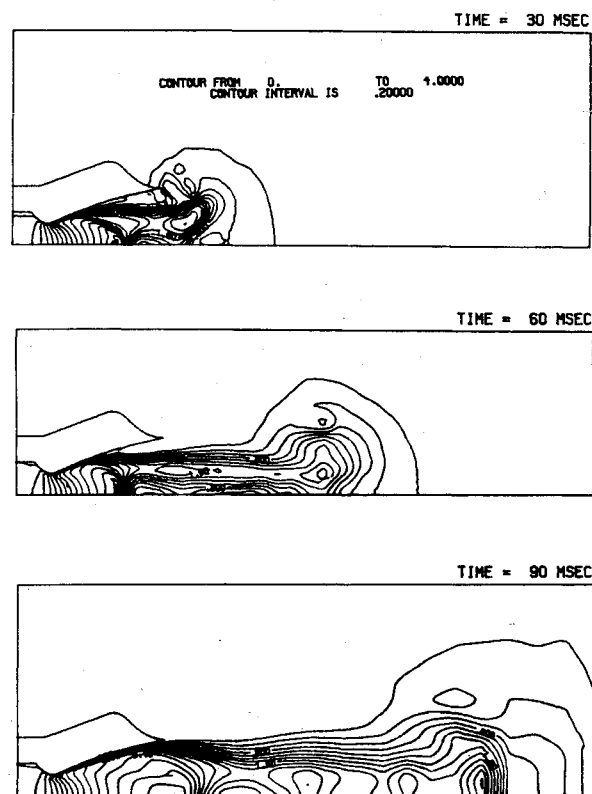**Fig. 6 Pressure vs time for the nonreflecting boundary condition study.**

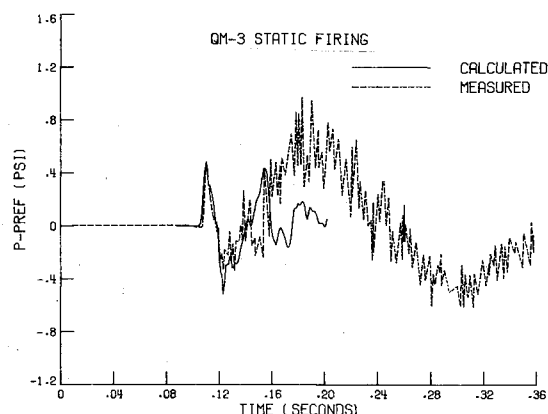**Fig. 7 Time sequence of Mach number contours (viscous) for the static firing case.**

Fig. 8 Calculated (viscous) and measured (unpublished Thiokol data) pressure vs time at the nozzle shroud for the static firing case.

Results

Calculations were made for both the static firing and STS-1 configurations. In both cases, the initial conditions consisted of zero velocity components, and the pressure and density equal to atmospheric values. Both calculations were begun at 85 ms, at which time the igniter shock wave burst the throat plug in the SRB nozzle, and continued until approximately 200 ms, at which time the second overpressure wave had reached a maximum. Both cases assumed the flow to be an ideal gas with the ratio of specific heats γ equal to 1.4 for the first 40 ms ($t = 85$-125 ms), varying linearly from 1.4 to 1.2 over the next 10 ms ($t = 125$-135 ms), and remaining constant at 1.2 for the rest of the calculation. The static firing case was calculated as both inviscid and viscous (turbulent) flow. The STS-1 case was calculated as inviscid, laminar, and turbulent flow. Only the inviscid and turbulent

flow results are presented although the laminar results are discussed.

Static Firing Case

Mach number contours for the viscous flow case are shown in Fig. 7. Each frame shows the flow at a specified time. The time shown on each frame of these plots, as well as all contour plots, is relative to the 85 ms starting time. From Figs. 7 and the additional results in Ref. 17, it can be seen that the flow initially enters the nozzle from the left and fills the diverging portion. The igniter wave is at the head end of this flow. This wave passes out of the nozzle and expands in what is roughly a spherical pattern. The flow then accelerates to sonic velocities in the throat region near the wall and supersonic velocities just downstream. The flow begins to separate from the nozzle wall just downstream of the throat region. This separation region then grows downstream until the whole diverging part of the nozzle is separated. This separation causes an oblique shock wave to form that extends downstream and reflects from the nozzle centerline as a Mach disk. Because the flow is separated just downstream of the throat, the exhaust jet downstream of the nozzle has a radius only slightly larger than the nozzle throat. As the chamber pressure builds, the separation point begins to move downstream causing the jet radius to grow. As the flow fills the nozzle, a second overpressure wave is generated by the downstream motion of the separation point and the radial motion of the exhaust jet. This overpressure wave travels out in a spherical pattern and passes over the nozzle shroud exiting the grid through the left-upper and upper boundaries. Because of the large pressure gradients in the nozzle region, the second overpressure wave does not show up very well in the pressure contour plots in Ref. 17. However, the high resolution color plots of Ref. 18 do show the formation of the second overpressure wave.

The computed pressure history for viscous flow at the nozzle shroud tip is compared with experiment in Fig. 8. The first pressure peak seen is the igniter wave produced in the actual firing just after rupture of the throat plug and is simulated well by the calculation using the specified initial chamber pressure transient. However, the second overpressure wave is too short in duration and somewhat reduced in magnitude. It is not clear why the calculated second overpressure wave is reduced in magnitude and duration when compared to experiment. One possible cause is the neglect of afterburning in the calculated results of the SRB nozzle exhaust. Another possible source of error is that the total pressure is measured using a stress gage on the SRB motor casing. This measured value was assumed to be constant across the nozzle inlet. Large variations of total pressure in the radial direction could delay the second overpressure wave significantly and, thus, increase its strength. Similar

arguments could be made for variations in total temperature. Other possible sources of error are turbulence modeling, neglect of the ground plane, and three-dimensional effects.

Comparing the viscous and inviscid solution Mach numbers, and pressure contour plots in Ref. 17, it can be seen that the inviscid solution does not provide a very realistic model of the flow. At 30 ms, the inviscid solution has a normal shock across the entire nozzle, while the viscous solution has an oblique shock and a Mach disk. As the viscous solution progresses, the Mach disk moves out into the exhaust jet, while in the inviscid solution the normal shock hangs on the nozzle exit lip. At 90 ms the inviscid solution is beginning to develop an oblique shock and Mach disk. A comparison of the calculated pressure for inviscid and viscous flow at the nozzle shroud tip is shown in Fig. 9. From Fig. 9, it can be seen that the inviscid solution produced a second overpressure wave one-fifth of that produced by the viscous solution. Other inviscid analyses[8] produced no second overpressure wave. Therefore, it an be seen that the inviscid equations do not correctly model the transient start-up of the SRB nozzle.

The inviscid and viscous flow solutions used 71×42 and 71×47 grid points and required 1.5 and 7.4 h of CPU time on the CDC-7600 computer, respectively. The inviscid flow calculations used the same grid as the viscous flow calculations except that the three grid points nearest the interior nozzle wall and the two nearest the exterior nozzle wall were removed. This results in a finer grid near the nozzle wall than is necessary for inviscid flow. However, this was done to minimize the differences between the inviscid and viscous flow grids and, thus to make a comparison of these two flows more meaningful. The same was true for the STS-1 case.

STS-1 Case

Mach number and pressure contours for the viscous flow case are shown in Figs. 10 and 11, respectively. Figure 10 shows that at 10 ms, the flow fills the nozzle and has separated from the nozzle wall forming an oblique shock and Mach disk at 20 ms. Between 30 and 40 ms, the separation point moves downstream. In the 50 ms frame, the separation point has moved upstream. At 60 ms, the separation point is again moving downstream. From 70 to 100 ms the separation point moves downstream and the flow again fills the nozzle. Figure 11 shows that at 10 ms, the igniter wave is in the nozzle. At 20 ms, this wave has left the nozzle and spreads out in a spherical pattern. Also, both incident and reflected shocks are present. At 30 ms, the igniter waves becomes very planar due to the interaction with the MLP wall. The reflected shock appears to break off and at 40 ms has moved downstream. At 50 ms, a second shock reflection from the centerline has formed. At 100 ms, the shock system has moved downstream of the nozzle exit and a third shock reflection from the centerline is forming.

During the early times these results closely resemble the static firing case. At later times the presence of the MLP hole wall decreases the spreading of the exhaust jet and increases the strength of the overpressure waves. This can be seen in Fig. 12, where pressure vs time at the top of the MLP hole are shown for both the static firing and STS-1 cases. From Fig. 12, it can be seen that the wall increases the waves but does not appear to be the source of any additional overpressure waves of significant strength.

The calculated results are compared to experiment in Fig. 13. The most outstanding feature of Fig. 13 is the absence of the igniter wave peak in the experimental data. This is because the experimental data have been filtered. To show the effect of this filtering process on the data, the filtered and unfiltered data for the static firing case are shown in Fig. 14 (unfiltered STS-1 flight data were unobtainable). From Fig. 14, it can be seen that filtering removes the igniter
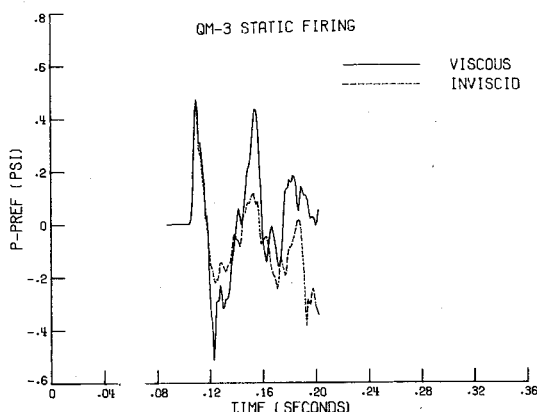

Fig. 9　Calculated pressure vs time at the nozzle shroud for the static firing case showing both inviscid and viscous flow.
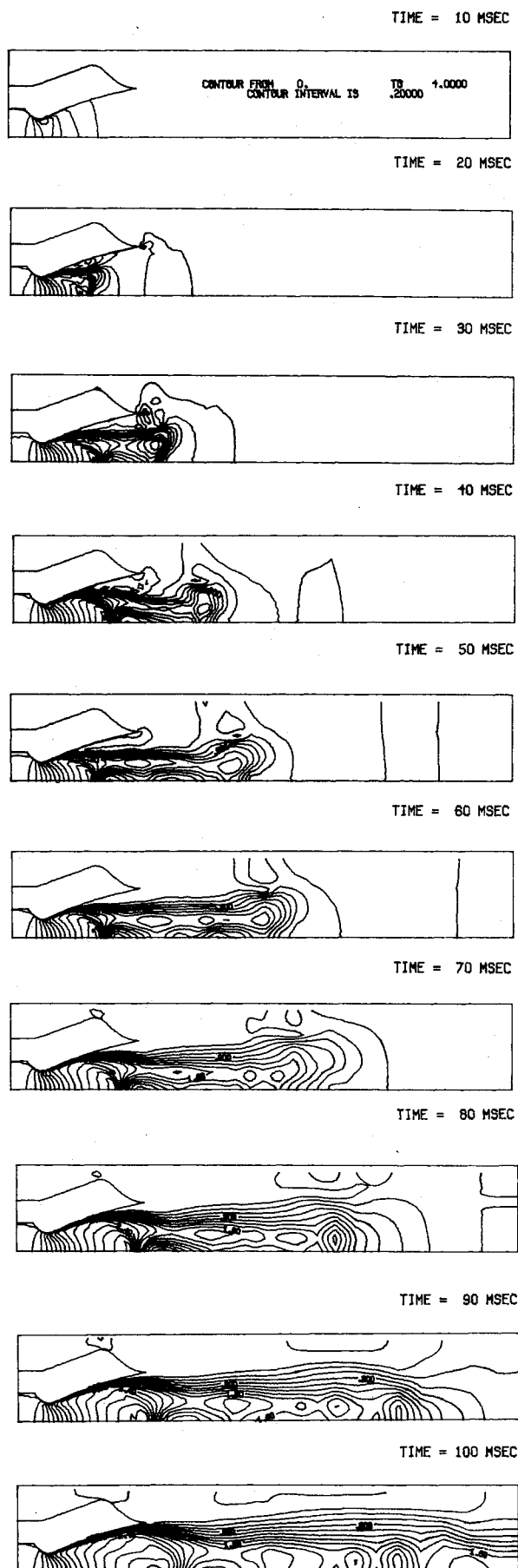
Fig. 10   Time sequence of Mach number contours (viscous) for the STS-1 case.
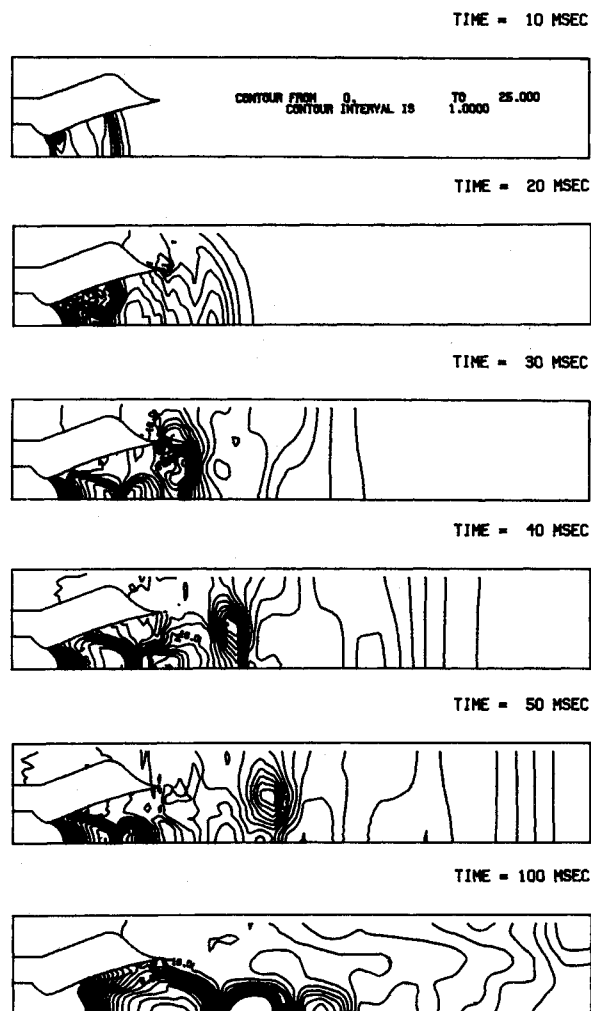

Fig. 11   Time sequence of pressure contours (viscous) for the STS-1 case.

wave spike. (Unfiltered data actually means data smoothed using a 1000 Hz filter, while filtered data had been generated using a 10-50 Hz filter.) Returning to Fig. 13, it can be seen that the computed results qualitatively predict the second overpressure wave. To determine the degree of agreement between the calculated and measured results requires running the calculation further in time. To date this has not been done for economic reasons as well as concerns that at later times the results may be influenced by reflections from the arbitrary computational boundaries. In addition to the possible sources of disagreement between computed and measured results mentioned for the static firing case, the disagreement in the STS-1 case may also be influenced by the effects of the rectangular MLP hole, water jets, and flame deflectors.

The computed inviscid and viscous flow solutions differences are similar to the static firing case for the early times. At late times, the static firing case inviscid and viscous flow differences seem to be lessening (see Ref. 17). However, this is not true in the STS-1 case. The comparison between inviscid and viscous solutions at 100 ms for the STS-1 case can be seen in Figs. 15 (Mach number contours) and 16 (pressure contours). From these figures it can be seen that in the viscous case, the exhaust jet extends downstream and exits the computational region with supersonic core flow. However, the inviscid flow solution still has a strong shock located at the nozzle exit with subsonic flow downstream.

Rather than forming a circular exhaust jet as in the viscous case, the inviscid flow solution appears to be forming an annular jet flowing out toward the MLP hole wall. Again, as in the static firing case, these results show how the inviscid equations are incapable of adequately describing this flow. The calculated pressure, for both inviscid and viscous flow, at the top of the MLP hole is shown in Fig. 17. Again, the inviscid solution produces a much reduced second overpressure wave. The inviscid results of Ref. 10 did not produce a second overpressure wave.

At this point it would be interesting to compare the viscous flow results presented herein with those of Ref. 10. However, Ref. 10 employed a C-type grid which causes very extreme grid spacing downstream of the nozzle, therefore, any detailed comparisons would be questionable. However, one comparison that may be useful is the direction of flow at the top of the MLP hole. In Ref. 10, the results indicate that at times greater than 70 ms, the entrainment of the exhaust jet is causing inflow at the top of the MLP hole. The present results indicated that the flow at the top of the MLP hole is directed upward and out of the hole. While the velocity magnitudes of the viscous flow results in the present study are less than the inviscid results, indicating that viscous entrainment is present, the velocity is still in an upward direction. This indicates that the viscous entrainment of Ref. 10, which is a laminar calculation, is greater than the present turbulent flow results. Because the actual MLP hole is rectangular, it is not possible to know which result is correct for the assumed two-dimensional geometry.

In addition to the viscous, turbulent flow calculation, a viscous, laminar flow calculation was also made for the STS-1 case. While the laminar flow results are similar to the turbulent flow results, the second overpressure wave is reduced in magnitude by approximately 25%.

The inviscid and viscous (turbulent) flow solutions used 71×22 and 71×27 grid points and required 0.8 and 6.3 h of CPU time on the CDC-7600 computer, respectively. The laminar flow solution used the same grid as the turbulent flow solution and required 5.0 h.

Fig. 14 Filtered and unfiltered measured (unpublished Thiokol data) pressure vs time at the nozzle shroud for the static firing case.

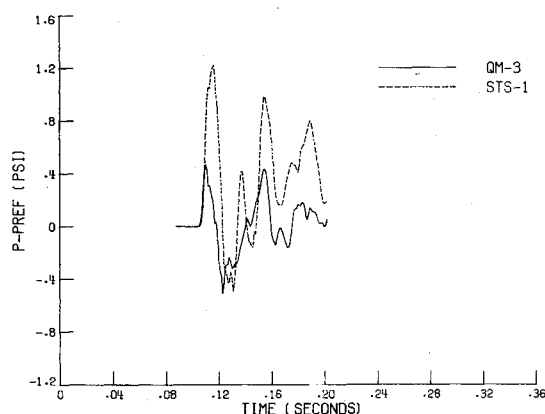Fig. 15 Mach number contours for the STS-1 case showing both inviscid and viscous flow.

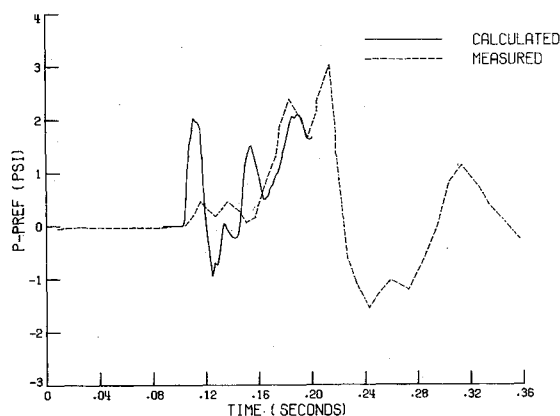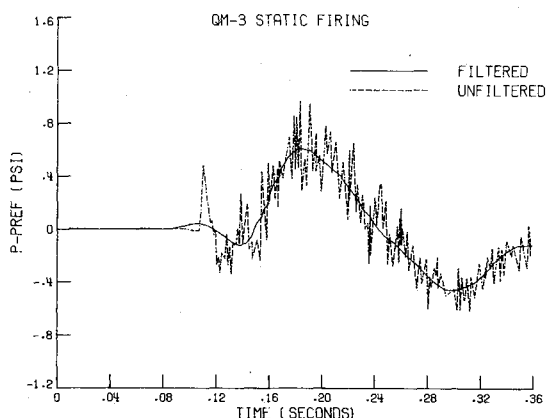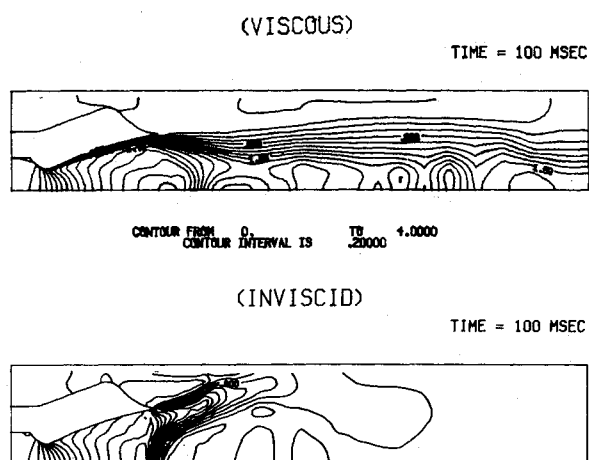Fig. 12 Calculated (viscous) pressure vs time at the nozzle shroud for both the static firing and STS-1 cases.

Fig. 13 Calculated (viscous) and measured (STS-1 flight data) pressure vs time at the top of the MLP hole wall for the STS-1 case.
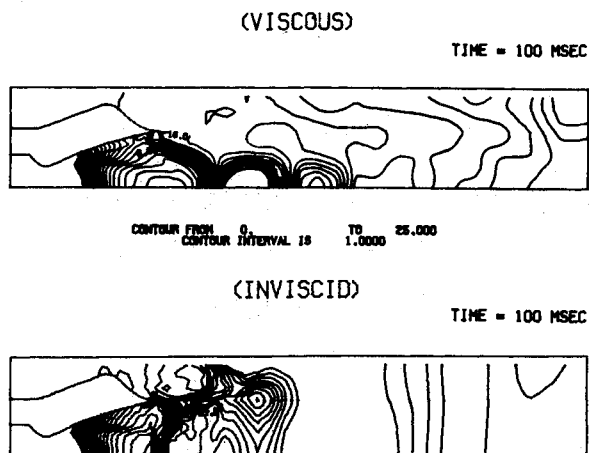

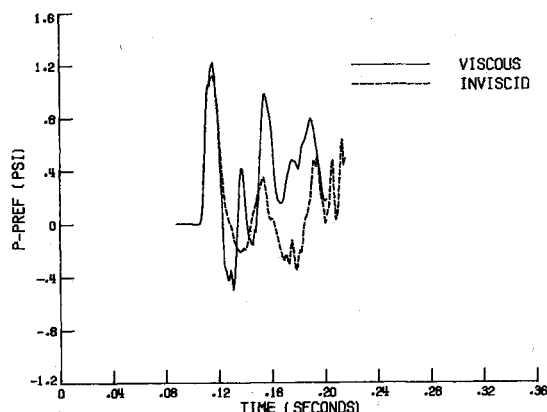Fig. 16 Pressure contours for the STS-1 case showing both inviscid and viscous flow.

Fig. 17   Calculated pressure vs time at the top of the MLP hole wall for the STS-1 case showing both inviscid and viscous flow.

Conclusions

Because of the qualitative agreement between theory and experiment, it has been concluded that the motion of the boundary-layer separation point and the subsequent radial motion of the exhaust jet cause a second overpressure wave. This wave is enhanced by the presence of the MLP hole wall. However, the presence of the wall does not appear to be the source of any additional overpressure waves.

The lack of good quantitative agreement between theory and experiment indicates that other overpressure sources, not accounted for by this simulation, may be present. Such other sources could be afterburning, nonuniform total pressure and temperature distributions at the nozzle inlet, turbulence modeling, and three-dimensional effects.

Comparisons of inviscid and viscous computed solutions indicate that the inviscid equations are incapable of adequately describing the SRB nozzle start-up transient flow.

Acknowledgments

This work was supported by the Propulsion Aerodynamics Branch of the NASA Langley Research Center and the U.S. Department of Energy.

The authors wish to thank Ernie Stampfl of the Aerospace Corporation for initially getting them involved with this project and providing much needed assistance during the early phases of this endeavor.

References

[1]McCarty, B. J., "Space Shuttle Flight Results," *Proceedings of the 1982 Annual Reliability and Maintainability Symposium,* Los Angeles, Calif., Jan. 1982.

[2]Cline, M. C., "VNAP2: A Computer Program for Computation of Two-Dimensional, Time-Dependent, Compressible, Turbulent Flow," Los Alamos National Laboratory, Los Alamos, N.M., Rept. LA-8872, Aug. 1981.

[3]Cline, M. C. and Wilmoth, R. G., "Computation of High Reynolds Number Internal/External Flows," *AIAA Journal,* Vol. 21, Feb. 1983, pp. 172-173.

[4]Broadwell, J. E. and Tsu, C. N., "Transient Pressures Caused by Rocket Start and Shutdown in Ducted Launches," *Journal of Spacecraft and Rockets,* Vol. 4, Oct. 1967, pp. 1323-1328.

[5]Peretz, A., Kuo, K. K., Caveny, L. H., and Summerfield, M., "Starting Transient of Solid-Propellant Rocket Motors with High Intenal Gas Velocities," *AIAA Journal,* Vol. 11, Dec. 1973, pp. 1719-1727.

[6]Salita, M., "Description of the Shock Waves Generated During the Initial Ignition Transient of the Space Shuttle Solid Rocket Boosters," Thiokol/Wasatch Div., Brigham City, Utah, Tech. Rept. TWR-13092, July 1981.

[7]Edwards, D. G. and Hillman, A., "Computations of Rocket Blast Fields," *5th International Symposium on Ballistics,* Toulouse, France, April 1980.

[8]Ndefo, E., Buell, J., Widhopf, G., and Murdock, J., "Space Shuttle SRB Ignition Overpressure Simulation," presented at the Shuttle Overpressure Workshop, JANNAF 13th Plume Technology Meeting, NASA Johnson Space Center, Houston, Tex., April 1982.

[9]Rapagnani, N. L. and Lutton, R. T., "Study of the Overpressure Effect on the STS Launch," presented at the Shuttle Overpresure Workshop, JANNAF 13th Plume Technology Meeting, NASA Johnson Space Center, Houston, Tex., April 1982.

[10]Li, C. P., "Numerical Investigation of Unsteady Flow Development in a Nozzle-Duct Configuration," AIAA Paper 83-1714, July 1983.

[11]Jones, W. P. and Launder, B. E., "The Calculation of Low-Reynolds-Number Phenomena with a Two-Equation Model of Turbulence," *International Journal of Heat and Mass Transfer,* Vol. 16, 1973, pp. 1119-1129.

[12]Hung, C. M. and MacCormack, R. W., "Numerical Solutions of Supersonic and Hypersonic Laminar Compression Corner Flows," *AIAA Journal,* Vol. 14, April 1976, pp. 475-481.

[13]MacCormack, R. W., "The Effect of Viscosity in Hypervelocity Impact Cratering," AIAA Paper 69-354, April 1969.

[14]Lai, S., "6.4 Per Cent Scale Model SSV SRM Ignition Overpressure Testing for STS-2, Vol. 2—Results of Analysis," Space Systems Group, Rockwell International, Downey, Calif., STS 81-0665, Jan. 1982.

[15]Caveny, L. H. and Kuo, K. K., "Ignition Transients of Large Segmented Solid Rocket Boosters," NASA CR-150162, April 1976.

[16]Rudy, D. H. and Strikwerda, J. C., "A Nonreflecting Outflow Boundary Condition for Subsonic Navier-Stokes Calculations," *Journal of Computational Physics,* Vol. 36, June 1980, pp. 55-70.

[17]Cline, M. C. and Wilmoth, R. C., "Computation of the Space Shuttle Solid Rocket Booster Nozzle Start-up Transient Flow," AIAA Paper 84-0462, Jan. 1984.

[18]Harlow, F. H. and Metropolis, N., "Computing and Computers," *Los Alamos Science,* Vol. 4, No. 7, Winter/Spring 1983, pp. 140-141.